ACS APPLIED MATERIALS & INTERFACES

Research Article

www.acsami.org

Revealing Amphiphilic Nanodomains of Anti-Biofouling Polymer Coatings

Carlo A. Amadei,[†,‡] Rong Yang,[†,§] Matteo Chiesa,*[,‡] Karen K. Gleason,[§] and Sergio Santos[⊥]

[‡]Institute Center for Future Energy (iFES), Masdar Institute of Science and Technology, Abu Dhabi, United Arab Emirates 54224
[§]Department of Chemical Engineering, Massachusetts Institute of Technology, Cambridge, Massachusetts 02139, United States
[⊥]Departament de Disseny I Programacio de Sistemes Electronics, Universitat Politecnica de Catalunya , Manresa, Spain 08242

Supporting Information

ABSTRACT: Undesired bacterial adhesion and biofilm formation on wetted surfaces leads to significant economic and environmental costs in various industries. Amphiphilic coatings with molecular hydrophilic and hydrophobic patches can mitigate such biofouling effectively in an environmentally friendly manner. The coatings are synthesized by copolymerizing (Hydroxyethyl)methacrylate and perfluorodecylacrylate via initiated chemical vapor deposition (iCVD). In previous studies, the size of the patches was estimated to be ∼1.4−1.75 nm by fitting protein adsorption data to a theoretical model. However, no direct observations of the molecular heterogeneity exist and therefore the origin of the fouling resistance of amphiphilic coatings remains unclear. Here, the amphiphilic nature is investigated by amplitude modulation atomic force microscopy (AM-AFM). High-resolution images obtained by penetrating and oscillating the AFM tip under the naturally present water layer with sub-nanometer amplitudes reveal, for the first time, the existence of amphiphilic nanodomains (1-2 nm^2). Compositional heterogeneity at the nanoscale is further corroborated by a statistical analysis on the data obtained with dynamic AM-AFM force spectroscopy. Variations in the long range attractive forces, responsible for water affinity, are also identified. These nanoscopic results on the polymers wettability are also confirmed by contact angle measurements (i.e., static and dynamic). The unprecedented ability to visualize the amphiphilic nanodomains as well as sub-nanometer crystalline structures provides strong evidence for the existence of previously postulated nanostructures, and sheds light on the underlying antifouling mechanism of amphiphilic chemistry.

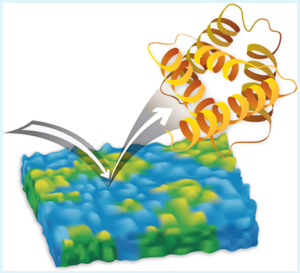

KEYWORDS: *amphiphilic, anti-biofouling, force reconstruction, molecular heterogeneity, SASS (small amplitude small set-point)*

INTRODUCTION

Surfaces that resist biomolecule and microbe adsorption are highly sought after for tissue engineering, medical implants and drug delivery systems, as well as for marine antifouling, water purification and desalination membranes, and other industrial applications.[1]

It is known that hydrophilic building blocks (i.e., ethylene glycol (PEG)6) or electrostatic hydrated zwitterionic groups[2] display low values of polymer/water interfacial energy, diminishing the adsorption of biofilms.[3] Nevertheless, hydrophobic membranes are widely used in industrial applications for their lower degradation rate and higher chemical stability compared to hydrated membranes.[4] A dichotomic anti-biofouling coating that displays solely hydrophilic or hydrophobic properties might not be adequate due to the intrinsic amphiphilic nature of large organism (i.e., bacteria) or biopolymer. On the other hand, surfaces with compositional heterogeneities have been hypothesized to resist adsorption, provided the length scale of surface domains is smaller than the region of contact between the foulant and the surface.[5,6] The alternation of hydrophilic and hydrophobic domains is postulated to limit thermodynamically favorable interactions (i.e., hydrophilic and hydrophobic interactions) between the foulant and the surface, hence reducing adsorption.[7−10] However, disruption of protein adsorption requires compositional heterogeneity at the nanoscale,[2,11] to create a mismatch between the nanodomains and the anchoring sites (i.e., footprint) of the protein.[12]

Amphiphilic protein-repellant surfaces have been successfully fabricated by copolymerization of hydrophilic (2-hydroxyethyl)methacrylate (HEMA) and hydrophobic (1H,1H,2H,2H-perfluorodecyl)acrylate (PFDA).[9] In this work, iCVD was used to synthesize thin films of the pure homopolymer pHEMA, the pure homopolymer pPFDA, and copolymers of HEMA and PFDA which spanned the entire compositional range in between. These surfaces were extensively characterized to determine composition, morphology, swellability, and contact angle properties. Additionally, uptake of bovine serum albumin (BSA) was experimentally quantified. On the hydrophilic pHEMA, the BSA uptake reduced by 75% as compared to the hydrophobic pPFDA. All of the amphiphilic surfaces measured displayed an even lower BSA uptake than pHEMA. The copolymer composition with 40% PFDA displayed the lowest BSA uptake, with a reduction

Received: November 16, 2013
Accepted: March 12, 2014
Published: March 12, 2014

   dx.doi.org/10.1021/am405159f | ACS Appl. Mater. Interfaces 2014, 6, 4705−4712

of 95% as compared to the pPFDA surface. In this initial study, the substrates were silicon wafers. In follow-up work, the same compositional range of thin films were deposited directly on the polymeric reverse osmosis membranes.[13] The ability of these CVD-coated membranes to resist bacterial adhesion was studied and again the copolymer deposited from the 40% PFDA provided the best antifouling performance.

BSA protein is a globular protein that exhibits a structure made of hydrophilic and hydrophobic patches.[14] BSA predominantly exposes hydrophilic patches toward the surface that are rich of hydrophilic residues and hydrophobic patches towards the interfaces which display hydrophobic nature. This phenomenon increases protein/surface interaction. In the case of copolymers, the creation of surface ambiguity with molecular heterogeneity comparable to the dimension of the patches limits favorable interactions. While these nanodomains responsible for the low protein adsorption were not directly visualized in the previous study,[9] a random lattice model was used to estimate the average size to be ∼1.4−1.75 nm. The model successfully explained the experimental observation of the minimal BSA adsorption with 40% PFDA content.

In the current work, we seek to provide direct visual evidence of nanoscale surface compositional domains on the iCVD amphiphilic surfaces (i.e., copolymer HEMA/PFDA). To achieve this goal, the investigation techniques must meet three requirements: (1) high lateral resolution imaging, i.e., ∼1−2 nm; (2) minimal sample invasiveness of soft matter; (3) spectroscopic-like capabilities for the identification of compositional heterogeneity and, possibly, for the detection of the accumulation of adsorbed water layers on the hydrophilic domains. To meet these requirements, we employ a recently reported[15] high-resolution and minimally invasive mode of amplitude modulation atomic force microscopy (AM-AFM) operated under ambient conditions, i.e., small amplitude small set-point (SASS). In this imaging mode, the cantilever oscillates near the surface with oscillation amplitude on the order of sub-nanometer (see Materials and Methods section). This allows resolving the molecular heterogeneities of random amphiphilic thin polymers, something not achievable with traditional imaging mode (i.e., non-contact NC mode). Requirements 2 and 3 are simultaneously addressed by employing phase contrast imaging and force spectroscopy while carefully controlling peak forces.[16] Furthermore, we define nanoscale observables that provide information about the presence or absence of chemical heterogeneity on the samples[17] and we corroborate these results with macroscopic contact angles measurements.

MATERIALS AND METHODS

Film Preparation and Derivatization. All iCVD films were deposited in a custom built vacuum reactor (Sharon Vacuum), as previously described.[2,18,19] Thermal excitations of the initiator were provided by heating a 0.5 mm nickel/chromium filament (80% Ni/20% Cr, Goodfellow) mounted in a parallel array and the temperature was measured by a thermocouple attached to one of the filaments. The filament holder straddled the deposition stage which was maintained at a set point temperature using water cooling. The vertical distance between the filament and the stage was 2 cm.

All the chemicals were used as purchased without further purification. Silicon (Si) wafers (Wafer World, test grade) were coated without pretreatment. During iCVD depositions, tert-butyl peroxide (TBPO, Aldrich, 97%) initiator and the nitrogen patch flow were fed to the reactor at room temperature through mass flow controllers (1479 MFC, MKS Instruments) at 1.5 and 1.1 sccm, respectively. 2-Hydroxyethyl methacrylate (HEMA, Aldrich, 97%) and 1H,1H,2H,2H-perfluorodecyl acrylate (PFDA, Aldrich, 97%) monomers were heated in a glass jars up to 75 and 80 °C, respectively, and delivered into the reactor using needle valves. Systematic variation of the flow rate ratios was performed to yield copolymers with various compositions. Films were deposited at a filament temperature of 250 °C and a stage temperature of 30 °C. Total pressure in the vacuum chamber was maintained at 0.121 Torr for all depositions.

In situ interferometry with a 633 nm HeNe laser source (JDS Uniphase) was used to monitor the film growth and deposit the desired thicknesses on Si substrates. A more accurate film thickness measurement on the Si wafer substrates was made post-deposition using a J.A. Woollam M-2000 spectroscopic ellipsometer at three different incidence angles (65, 70, 75°) using 190 wavelengths from 315 to 718 nm. The data were fit using a Cauchy−Urbach model.

SASS Imaging. Recently, two groups[15,20] have independently demonstrated that it is possible to scan under the water layer universally present when a surface is exposed to ambient condition. This allows increasing resolution and minimizing conservative and dissipative peak forces.[21] Remarkably similar results have been shown in the two common modes of dynamic operation respectively, namely AM[15] and frequency modulation FM AFM.[20] One of these two modes is referred as Small Amplitude Small Set-point (SASS). SASS has been shown to maximize resolution[15] without the requirement of intrinsic 3-dimensional lattice periodicity[22−24] or sufficient stiffness of the sample.[25] SASS technique consists in imaging with sub-nanometer oscillation amplitudes, free amplitudes in the range of 1−5 nm and sharp tips with radii smaller than 5 nm. Under these conditions, the tip oscillates in the proximity of the surface. Moreover, small cantilevers (OLYMPUS 55TS) were employed to reduce thermal noise while imaging in SASS.[26] Although these cantilevers were very stiff, i.e., $k \approx$ 170 N/m, the maximum energy dissipated per cycle in SASS was less than 1.7 eV throughout.

Reconstruction of Force Profile in AM AFM. The ability to recover the tip-sample interaction as a function of tip-sample distance (d_m) from observables is generally defined as the reconstruction of nanoscale force profile.

The experiments have been carried out using Asylum Research Cypher Scanning Probe Microscope. The silicon cantilevers' parameters (OLYMPUS 55TS) are $k \approx 150$ N/m, $Q \approx 700$, $f = f_0 \approx$ 1.9 MHz, and $R \leq 5$ nm. The size of the tip (R) has been constantly monitored in situ by following the onset of the transition from the attractive to the repulsive regime, i.e., A_C method.[27] The force reconstruction exploits Katan−Sader−Jarvis formalism[28] (eq 2) in which the force versus distance profile is recovered from the variations in the frequency shift Ω that occur by decreasing the cantilever-sample separation (z_c). Then from z_c is possible to obtain the tip/sample distance d_m by subtracting the perturbed oscillation amplitude A

$$d_{min} \approx z_c - A \tag{1}$$

The normalized conservative force F_{ts}* as function of d_m reads

$$F_{ts}^*(d_m) = \frac{2k}{|F_{AD}|}\int_{u=d_m}^{u=\infty}\left[\left(1+\frac{A^{1/2}}{8\sqrt{\pi(u-d_m)}}\right)\Omega(u) - \frac{A^{3/2}}{\sqrt{2(u-d_m)}}\frac{d\Omega(u)}{du}\right]du \tag{2}$$

where the force has been normalized with the absolute value of the force of adhesion $|F_{AD}|$ and where Ω is the normalized frequency expressed by

$$\Omega(d_m) = \left[1+\frac{A_0}{QA}\cos(\Phi(d_m))\right]^{1/2} - 1 \tag{3}$$

In eq 3, A_0 is the free or unperturbed amplitude of oscillation and Φ is the phase lag relative to the driving force. The free amplitude, A_0, is a key parameter to avoid bistability and discontinuity in the amplitude-

Table 1. HEMA and PFDA Content for the Four Polymers[a]

type	label	% PFDA	% HEMA	normalized protein adsorption (%)[b]	static contact angle (deg)	advancing contact angle (deg)	receding contact angle (deg)	hysteresis contact angle (deg)
hydrophilic homopolymer	F0	0	100	25	65.8 ± 2.1	82.3 ± 0.9	22.5 ± 1.4	59.3 ± 1.3
amphiphilic copolymer	F40	40	60	5	115.1 ± 0.5	122.1 ± 0.3	26 ± 1.8	96.1 ± 1.5
amphiphilic copolymer	F75	75	25	20	123.0 ± 0.2	123.4 ± 0.6	70.7 ± 1.7	52.7 ± 1.6
hydrophobic homopolymer	F100	100	0	100	123.2 ± 0.6	128.7 ± 0.4	81 ± 2	45 ± 4

[a]Protein adsorption data are normalized. 100% protein adsorption data correspond to 500 ng/cm^2. [b]The normalized protein adsorption data refer to the previous study.[9].

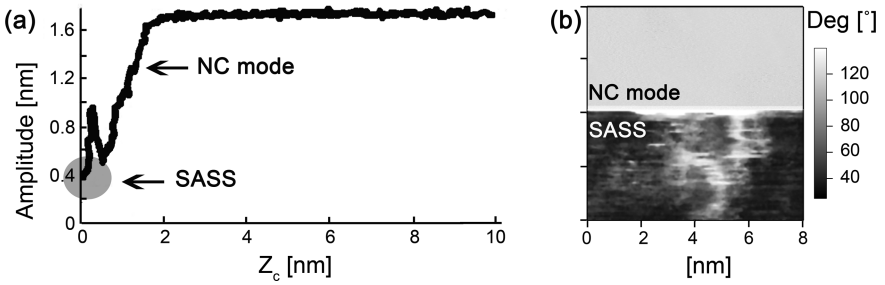

Figure 1. (a) Experimental amplitude curve obtained as a function of cantilever separation z_c with a standard AC55TS (OLYMPUS) cantilever on the F75. (b) Phase contrast channel shows that nanoscale structures with lateral dimensions on the order of 1 nm are resolved in the SASS mode of imaging (bottom of the image contrast >60°), whereas no contrast is observed in the NC mode (top of the image contrast <0.5°)). The transition from NC mode to the SASS mode was induced by simply reducing the set point from ∼1.5 nm (NC mode) to ∼0.4 nm (SASS mode) as predicted in a. The free amplitude was $A_0 \approx 1.7$ nm.

phase-distance (APD) curves. For *OLYMPUS 55TS*, the value of A_0 needed to avoid bistability was less than 5 nm.

The normalized energy dissipated per cycle, E_{dis}*, is estimated with the standard equation[29,30]

$$E_{dis}^{*} = \frac{\pi k A_0 A}{E_{dis}(\max) Q}\left[\sin(\Phi) - \frac{A}{A_0}\right] \quad (4)$$

where E_{dis}(max) corresponds to maxima in the APD curve, and can be plotted versus d_m to highlight particular long range dissipative process (i.e., capillary).

Contact Angle Measurements. The contact angle measurements were executed with a Krüss FM40Mk2 EasyDrop contact angle instrument. In particular, static contact angles were measured using 2 μL DI water droplets. The data for each polymer refers to a series of 5 measurements. Advancing and receding contact angles were measured by recording the advancing and receding of the contact line, while increasing or decreasing the droplet volume by means of the sessile drop method.[31] The initial volume was set to 2 μL and the volume of the droplet is increased up to 5μL, after which the receding phase was evaluated.

RESULTS AND DISCUSSION

Table 1 summarizes the HEMA and PFDA content for the four polymers investigated in this work. In particular, each polymer has been labeled in respect to its hydrophobic content (i.e., for F40 the hydrophobic content is equal to 40%).

In the previous study,[9] protein adsorption onto the polymer films was measured by a quartz crystal microbalance with dissipation monitoring (QCM-D, model E4, Q-sense). This previous work showed that the amphiphilic copolymer, F40 was superior in resisting BSA protein adsorption as compared to either the hydrophilic (F0) or hydrophobic homopolymers (F100), respectively.[9] The normalized protein adsorption results are summarized in Table 1. We note that the hydrophobic homopolymer is characterized by the higher protein adsorption. This is due to the fact that apolar surfaces destabilize the BSA proteins, facilitating their unfolding, and leading to strong inter-protein and protein−surface interactions.[32]

It can be argued that imaging in the NC mode of operation in AM AFM is preferable for soft matter imaging.[16] The NC mode is experimentally reached by sufficiently decreasing the free amplitude, i.e., typically ∼1 nm, while keeping the set-point as high as possible.[33] On average, in the NC mode, the tip oscillates higher above the sample so there is no mechanical contact and/or sample deformation.[33] A drawback of the NC imaging mode is that compositional contrast via the phase channel might be limited or minimal. A second drawback is the origin of contrast in NC imaging mode even in topography, i.e., long range unlocalized interactions. Unlocalized interactions (i.e., van der Waals) limit lateral resolution and might even negatively affect apparent height reconstruction.[34] The limitations of NC mode imaging might be particularly pronounced in ambient conditions since nanoscale water films covering the tip's and the sample's surfaces screen the forces originating from the sample.[35] In a nutshell, traditional NC imaging methods (Figure 1b, top) are limited in resolution since they operate with long range nonlocalized forces and therefore are not appropriate for visualizing nano- and subnano-scale features. On the other hand, thanks to its sub-nanometer oscillation amplitudes, SASS mode of operation is sensitive to more localized forces and, as seen in Figure 1b, bottom, it can resolve nanodomains on the copolymer (i.e., F75) with phase contrast of more than 20°. In Figure 1b, the transition from the NC mode ($A_{sp} \approx 1.5$ nm) to the SASS mode ($A_{sp} \approx 0.4$ nm) was induced while acquiring the image by sufficiently reducing the oscillation amplitude A_{sp} (Figure 1a)

while keeping A_0 constant at $A_0 \approx 1.7$ nm as recently reported.[15]

The SASS mode was then utilized to acquire 10 × 10 nm phase images with 256 × 256 pixel resolution (Figure 2) for the 4 polymers listed in Table 1. Phase contrast is sensitive to surface compositional variation and it can be converted to energy dissipation maps between the tip and the surface during each oscillation cycle.[36,29] Phase contrast images have been employed here on all the coatings with various compositions. While several images in SASS were obtained for each polymer, those shown in Figure 2 are representative scans of the coatings and therefore are the focus of the following discussion.

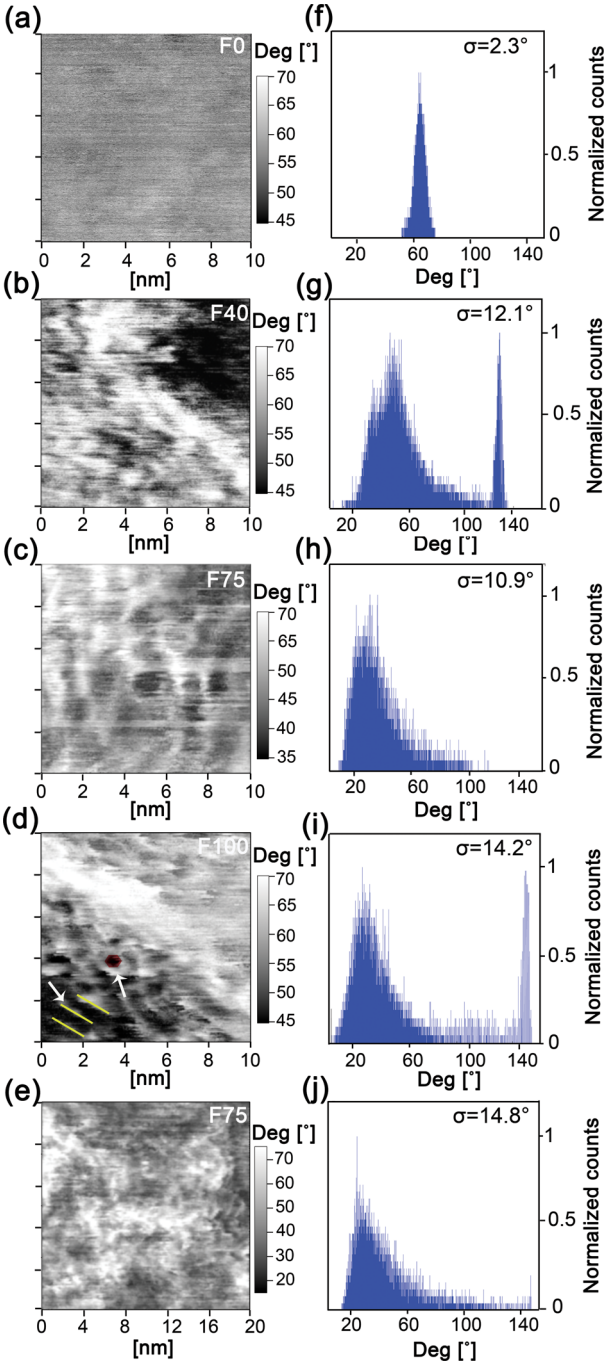

Figure 2. 10 × 10 nm phase images of the (a) F0, (b) F40, (c) F75, (d) F100. All images have been obtained in the SASS mode and with tips with radii of 5 nm or less. In (a), the phase image presents contrast of less than 2°, whereas (b)−(d) show nano domains (1−2 nm^2) with greater contrast, i.e., ∼10°. (e) Phase image of F75. The size of the domains is consistent and scales with a larger scan areas (20 × 20 nm) as shown in (e). In (d), hexagonal packings of perfluorinated side chains in PFDA repeat units have been highlighted in red and lamellar structures in yellow. Parameters: $A_0 \approx 1$ nm, $A_{sp} \approx 0.3$ nm, and scan rate 1 Hz. (f)−(j) Histograms representing the distribution of the phase contrast of images (a)−(e), respectively.

Hydrophilic homopolymer (F0, Figure 2a). The phase contrast is not significant for F0 compared to F40 (Figure 2b), F75 (Figure 2c), and F100 (Figure 2d), even in SASS. The distribution of phase values is shown in Figure 2f with the mean value at ∼65°. This coating composition has the lowest standard deviation in phase contrast out of the four coating compositions, i.e., σ = 2.3°. The qualitative observations and quantitative results obtained for this sample are in accordance with the homogeneous chemical composition of the surface. Thus, these results can be regarded as direct evidence of the absence of nanoscale domains in terms of compositional variations or heterogeneity.

Amphiphilic Copolymers (F40, Figure 2b, and F75, Figure 2c, e). The images display domains on the order of 1−2 nm^2. Furthermore, the phase values are broadly distributed (Figure 2f, g), indicating that the origin of the contrast is compositional heterogeneity. The broadened distribution of phase values is evidenced quantitatively by the standard deviations values of 12.1° for F40 and 10.9° for F75; the 95th percentiles are 58.3 and 75.2° for F40 and F75, respectively. The enhanced phase contrast confirms the surface chemical heterogeneity characteristic of the copolymers P(HEMA-*co*-PFDA), whereas the nanoscale dimensions of the domains are confirmed from dimensions of the features in the phase images, which are measured to be 1−2 nm^2.[11] This size is consistent with the values inferred from a random lattice model (i.e., 1.4−1.75 nm).[9,37] In summary, the combination of these findings supports a correlation between the presence of chemical heterogeneous nanodomains and low values of protein adsorption for the copolymers. The nanodomains thermodynamically discourage the adsorption of protein due to low surface/protein interaction. Moreover, the heterogeneity minimizes protein conformational re-organization. If this reorganization had happened, the protein would have increased its entropy, leading to a spontaneous adsorption process (i.e., variations in the Gibbs free energy less than zero).[38] In Figure 2e, an increased scanning area (20 × 20 nm) for the F75 copolymer also shows the nanodomains structure. Thus, these results can be regarded as direct evidence of the presence of nanoscale domains in terms of compositional variations or heterogeneity.

Hydrophobic Homopolymer (F100, Figure 2d). Surprisingly, significant phase contrast is also observed for this homopolymer. The images reveal unique lamellar (yellow lines) and hexagonal features (red hexagon) pointed out with the arrows. The standard deviation here is approximately 14.2° (Figure 2i). The phase contrast here can be explained by the tendency of the iCVD pPFDA polymers to form crystalline structures. The mesomorphic state of the heptadecafluorodecyl (C_8F_{17}) group in the side chain of a PFDA repeat unit has an ordered smectic liquid crystalline (LC) structure in the Smectic B phase consisting of a succession of bilayers (see Figure S2 in Supporting Information).[39,40] Each bilayer is composed of two heptadecafluorodecyl groups without interpenetrating and thus has the characteristic thickness of 3.2 nm, precisely twice the

length of extended heptadecafluorodecyl groups[37] The heptadecafluorodecyl groups are oriented perpendicularly to the polymer backbones (grey entangled lines in Figure S2 in the Supporting Information) and exhibit hexagonal packing with a lattice parameter of 0.64 nm.

It is also worth mentioning that the peaks centered at 130 and 150° in histograms 2g and 2i, respectively, do not express true phase contrast and are interpret as outliers. This is corroborated by comparing the population of the intervals 130 ± 10° and 150 ± 10°. These intervals represent, in both cases, less than 1% of the entire population, and the peaks can be attributed to instabilities or feedback errors during the scans due to topography induced transient amplitudes. Thus, these peaks do not refer to a variation in the surface composition. Furthermore, a non-zero standard deviation in phase can follow from errors related to thermal excitation, i.e., typically ∼0.5−1° in our experiments, or feedback. Here feedback errors were minimized by keeping the scan axis at speeds below 20 nm/s as discussed in detail below.

It could be argued that the phase contrast observed in Figure 2b-e could have been an artifact of the non-ideal response of the feedback loop,[29,41] related to the coupling of phase with topography. In order to minimize this effect, small errors in the amplitude signal (maxima ∼10 pm) were achieved by (1) scanning rate of 20 nm/s or less in the scan axis, (2) choosing an appropriate number of pixels per scan to allow resolving domains of 0.01 nm^2 or less (pixel size <0.01 nm^2), (3) carefully tuning the feedback gains for optimum tracking. Moreover, a correlation study (see Figure S1 in the Supporting Information) between the height (topography) and the phase signals has been carried out in order to confirm the lack of correlation (Pearson product-moment correlation coefficient PCC) between the two observables. In summary, the PCC (see Figure S1 in the Supporting Information) is centered at zero in all cases giving r = 0.05, −0.18, 0.02, and −0.08 for the images in Figure 2a−d, respectively. These results confirm that any phase contrast in the images above is related to compositional heterogeneity in the nanoscale rather than error related artifacts.

Note that nanodomains were also resolved in a previous study by means of scanning electron microscopy.[6] In particular, the authors reported larger domain dimensions than those reported here but they did not exclude the possible presence of the smaller domains. Further confirmation of the presence of heterogeneous nanodomains is given by employing force spectroscopy measurements in AM-AFM. In particular, recently proposed force spectroscopy methods[17,42] are exploited to identify compositional heterogeneity in the nanoscale and, possibly, the source of fouling resistance. Conservative and dissipative interactions are recovered as a function of minimum distance of approach d_m (see Materials and Methods section). This allows increasing the number of observables such as F_{AD}, ΔdF_{AD} and $\Delta\Phi^*$. The force of adhesion F_{AD} represents the minimum value in the conservative force and is an important parameter that distinguishes surface heterogeneity.[43] Small variations of F_{AD} can indicate chemically homogeneous surfaces. ΔdF_{AD}, defined as a distance ΔdF_{AD} for which $F_{ts}^* \leq 0.8|F_{AD}|$, can represent a footprint of nanoscale adsorbed water layer,[42] reaching values on the order of 1 nm when adsorbed water films are present on the surface.[42] The arbitrary value 0.8 has been chosen to tolerate a certain level of noise due to reconstruction of force profiles. ΔdF_{AD} can also be employed to qualitatively discriminate between nanoscale variations in terms of the surface energy of a material. For example, ΔdF_{AD} will vary as water adsorbs on a surface[38] and constant ΔdF_{AD} values should follow from homogeneity of surface properties. However, if the sample displays heterogeneity in terms of surface energy this will translate into large variations in ΔdF_{AD} when measurements are acquired on different regions of the surface.[42] Steplike variations in the normalized phase difference $\Delta\Phi^*$, which occur before mechanical contact between the tip and the surface is established (d_m > 0 nm), are related to capillary phenomena and thus to the presence of adsorbed water on the surface.[42,44]

Figure 3 shows the Fts* (red lines) and $\Delta\Phi^*$ (black line) versus the minimum distance between the tip and the surface

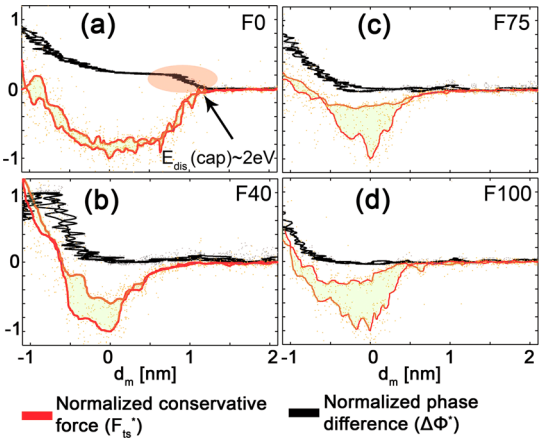

Figure 3. Normalized conservative force (Fts*, red lines) and normalized phase difference signal ($\Delta\Phi^*$, black lines) as a function of d_m. (a) F0, (b) F40, (c) F75, (d) F100. Data were acquired at random spots in each surface. For each sample the most dissimilar results are plotted. Larger green areas imply large variations or heterogeneity in terms of the conservative force profile (b)−(d). All plots show similar dissipative processes via the normalized phase difference $\Delta\Phi^*$ signals (black lines) since these overlap. $\Delta\Phi^* \approx 0$ implies zero dissipation showing that in (b)−(d), dissipation occurs mainly after mechanical contact between the tip and the sample ($\Delta\Phi^* \approx 0$ for $d_m > 0$). (a) F0 presents long range dissipative processes with $\Delta\Phi^* > 0$ for $d_m > 0$ (labeled with a red ellipse). |Fts| (minima) ranging between 0.63/0.65, 0.22/0.56, 0.16/0.33, 0.39/1.32 nN and $\Delta\Phi$ (maxima) ≈ 36°/38°, 8°/9°, 8°/9°, 9°/11°, for samples (a)−(d), respectively. The largest values have been employed to normalize the y axes in each figure. The reference value d_m = 0 nm has been taken as coinciding with minima in Fts* and thus indicating the point of mechanical contact.

d_m. The data have been obtained from experimental amplitude-phase-distance (APD) curves acquired at several spots on the four samples. In each figure the two most dissimilar phase and force versus distance profiles, obtained from 100 APD curves randomly acquired on the surface of each polymer, are plotted. Note that because $\Delta\Phi^*$ can be directly related to energy dissipation,[44] the overlapping of $\Delta\Phi^*$ in the figures represents homogeneous energy dissipation profiles[30](see Materials and Methods section). It is only for the F0 homopolymer that a steplike variation ($\Delta\Phi \approx 6°$), highlighted with a red ellipse in Figure 3a, is observed. This signal indicates the presence of capillary interactions and is consistent with the hydrophilic nature of the homopolymer (static contact angle = 65.8 ± 2.1°) and the presence of nanoscale water films on the surface. The corresponding energy dissipation is E_{dis}(cap) ≈ 2 eV, where cap stands for capillary. This value is in accordance with those

dx.doi.org/10.1021/am405159f | ACS Appl. Mater. Interfaces 2014, 6, 4705−4712

typically reported in the literature for such phenomena with the use of sharp tips, i.e., $R \leq 5$ nm, as employed here.[45] Conversely, for the three samples containing the hydrophobic compound (PFDA) $\Delta\Phi^* \approx 0$ in the long range, i.e., $d_m > 0$. The lack of long range dissipation, including capillary dissipation, agrees with the intrinsic non-wetting macroscale nature of the three samples, as confirmed by static contact angle measurements (Table 1); F40, F75, and F100 assume static contact angles of 115 ± 0.5°, 123 ± 0.2°, and 123 ± 0.6°, respectively. Dynamic contact angles confirm the nonwetting behavior of these three polymers. In particular, for all three polymers the advancing contact angle reaches a value of approximately 125°. However, F40 polymer is characterized by a receding contact angle of 26 ± 1.8°, which is significantly lower compared to those of F75 and F100. The low receding contact angle of F40 leads to a high degree of contact angle hysteresis (i.e., 96.1 ± 1.5°). It is widely acknowledged that high values of contact angle hysteresis are caused by the presence of regions with contrasting surface properties or by surface roughness.[31,46] In our case, we can disregard the second reason, since the roughness of F40 is similar to that of F75 and F100. (Figure S3 in Supporting Information). Other reason behind high values of contact angle hysteresis might be connected to surface reconstruction at the film−water interface.[47] In particular, after contact with water, the surfaces might reconstruct so that the hydroxyl moieties preferentially orient outward and the fluorinated moieties preferentially orient inward.

Contrary to the phase signal, the conservative force F_{ts}* profiles show remarkable variations (green areas in Figure 3) for the polymers containing the hydrophobic matrix. These variations can be quantified by a statistical study based on ΔdF_{AD} (left side Figure 4) and F_{AD} (right side of Figure 4) as obtained from the APD population curves. First, note that only the hydrophilic homopolymer, F0, displays a narrow distribution in F_{AD} (i.e., relative standard deviation 3.6%) centered at 0.64 nN. This provides further confirmation regarding the homogeneous chemical nature of the surface and the absence of heterogeneous nanoscale domains. The other three samples reflect their compositional heterogeneity yielding a broader distribution in terms of F_{AD} (i.e., relative standard deviation 24.7, 25.6, and 26.1% for the F40, F75, F100 respectively). These stochastic variations in local surface chemical composition, as quantified by $F_{AD,}$ corroborate the findings obtained from phase contrast images in SASS (Figure 2b−e). Second, in terms of ΔdF_{AD}, it can be observed that the F0 homopolymer is characterized by a distribution centered at 1.08 nm (Figure 4a) with relative standard deviations of 13.9%, which is indicative of a uniform grade of wettability. For the F40, F75, and F100 polymers, average values of ΔdF_{AD} are on the order of subnanometer. These values are closer to those obtained in the absence of nanoscale water films. Standard deviations are 25.9, 29.8, and 37.5% for F40, F75, and F100, respectively. Variations in ΔdF_{AD}, i.e., standard deviations ∼20−40%, might relate to heterogeneity in nanoscale wetting and heterogeneous surface energy (copolymers) or inherent chemical structures that compose the pPFDA homopolymer, F100, as detailed above when discussing Figure 2d. The presence of heterogeneity in terms of surface energy discourages any kind of interaction between proteins and polymers as has been confirmed in previous studies conducted with other techniques (i.e., NEXFAS spectroscopy).[48]

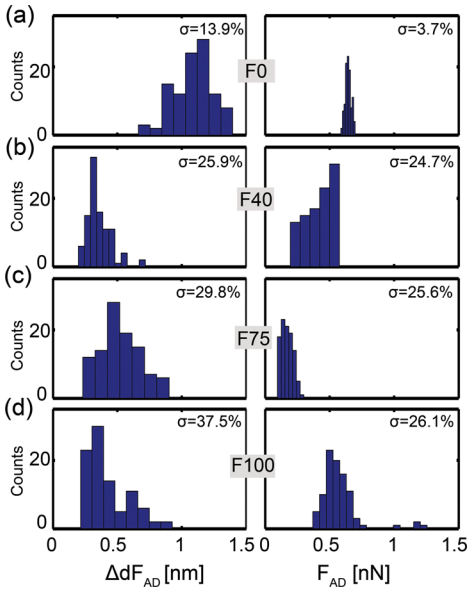

Figure 4. Histograms of the population of force curves taken randomly on each sample: (a) F0, (b) F40, (c) F75, (d) F100. For each sample the force of adhesion (F_{AD}) and distance ΔdF_{AD} are shown. Smaller variations in F_{AD} and larger values of ΔdF_{AD} are observed for the 100% hydrophilic homopolymer (F0, a) as compared to the 100% hydrophobic polymer (F100, d).

CONCLUSIONS

The presence of nanodomains has been confirmed on amphiphilic coatings by employing a minimally invasive and high resolution mode of AM-AFM with SASS under ambient conditions. In particular, it has been demonstrated that the surfaces of the amphiphilic copolymers (i.e., F40, F75) consist of nanoscale domains of compositional heterogeneity. Heterogeneity is also found in these samples in terms of their ability to form nanoscale water films. However, water films patches on the amphiphilic coating are not sufficiently large in the xy plane to induce capillary phenomena.[49] In summary, the exceptionally fine resolution of the AM-AFM with SASS operation mode enabled the visualization of nanometer and subnanometer domains in amphiphilic copolymers for the first time. This provides direct evidence of the unique film morphology and sheds light on the nature and origin of the fouling resistance of amphiphilic chemistry. The sub-nanometer crystalline structures are also resolved nicely with the AM-AFM technique. This is the first observation of crystalline structures of all iCVD thin film coatings, which is corroborated by XRD measurements. The unprecedented high-resolution mapping of molecular domains with simultaneous spectroscopic capabilities resolves the long-lasting challenge of direct visualization of molecular structures and can serve as a powerful tool in the fast-growing fields of nanofabrication and nanotechnology.

ASSOCIATED CONTENT

Supporting Information

Additional figures and results discussion on the correlation between AFM topography/phase and X-ray analysis. This material is available free of charge via the Internet at http://pubs.acs.org/.

AUTHOR INFORMATION

Corresponding Author

*E-mail: mchiesa@masdsar.ac.ae.

Author Contributions

†Authors C.A.A. and R.Y. contributed equally to this work.

Notes

The authors declare no competing financial interest.

ACKNOWLEDGMENTS

We thank Maritsa Kissamitaki and Martí de Cabo Jaume for producing the visual abstract and figures. C.M. gratefully acknowledges the support of the Masdar Institute in funding this research. K.K.G. and R.Y. thank the King Fahd University of Petroleum and Minerals in Dhahran, Saudi Arabia, for funding the research reported in this paper through the Center for Clean Water and Clean Energy at MIT and acknowledge the support from DOE Office of ARPA-E under Award AR0000294.

REFERENCES

(1) Banerjee, I.; Pangule, R. C.; Kane, R. S. Antifouling Coatings: Recent Developments in the Design of Surfaces That Prevent Fouling by Proteins, Bacteria, and Marine Organisms. *Adv. Mater.* **2011**, *23* (6), 690−718.

(2) Yang, R.; Jingjing, X.; Ozaydin-Ince, G.; Wong, S. Y.; Gleason, K. K. Surface-Tethered Zwitterionic Ultrathin Antifouling Coatings on Reverse Osmosis Membranes by Initiated Chemical Vapor Deposition. *Chem. Mater.* **2011**, *3*, 1263−1272.

(3) Werner, C.; Maitz, M. F.; Sperling, C., Current Strategies Towards Hemocompatible Coatings. *J. Mater. Chem.* **2007**, *17*.

(4) Yun-Feng, Y.; Yang, L.; Qing-Lian, L.; Ling-Shu, W.; Xu, Z.-K. Surface Hydrophilization of Microporus Polyprpylene Membrane by Grafting Zwitterionic Polymer for Anti-Biofoluing. *J. Membr. Sci.* **2010**, *362*, 255−264.

(5) Weinman, C. J.; Gunari, N.; Krishnan, S.; Dong, R.; Paik, M. Y.; Sohn, K. E.; Walker, G. C.; Kramer, E. J.; Fischer, D. A.; Ober, C. K. Protein Adsorption Resistance of Anti-Biofouling Block Copolymers Containing Amphiphilic Side Chains. *Soft Matter* **2010**, *6*, 3237−3243.

(6) Wong, S. Y.; Han, L.; Timachova, K.; Veselinovic, J.; Hyder, M. N.; Ortiz, C.; Klibanov, A. M.; Hammond, P. T. Drastically Lowered Protein Adsorption on Microbicidal Hydrophobic/Hydrophilic Polyelectrolyte Multilayers. *Biomacromolecules* **2012**, *13*, 719−726.

(7) Krishnan, S.; Ayothi, R.; Hexemer, A.; Finlay, J. A.; Sohn, K. E.; Perry, R.; Ober, C. K.; Kramer, E. J.; Callow, M. E.; Callow, J. A.; Fischer, D. A. Anti-Biofouling Properties of Comblike Block Copolymers with Amphiphilic Side Chains. *Langmuir* **2006**, *22*, 5075−5086.

(8) Finlay, J. A.; Krishnan, S.; Callow, M. E.; Callow, J. A.; Dong, R.; Asgill, N.; Wong, K.; Kramer, E. J.; Ober, C. K. Settlement of Ulva Zoospores on Patterned Fluorinated and PEGylated Monolayer Surfaces. *Langmuir* **2007**, *24*, 503−510.

(9) Baxamusa, S. H.; Gleason, K. K. Random Copolymer Films with Molecular-Scale Compositional Heterogeneities that Interfere with Protein Adsorption. *Adv. Funct. Mater.* **2009**, *19*, 3489−3496.

(10) Zhao, Z.; Ni, H.; Han, Z.; Jiang, T.; Xu, Y.; Lu, X.; Ye, P. Effect of Surface Compositional Heterogeneities and Microphase Segregation of Fluorinated Amphiphilic Copolymers on Antifouling Performance. *ACS Appl. Mater. Interfaces* **2013**, *5*, 7808−7818.

(11) Macritchie, F., Protein at Interfaces. *Adv. Protein Chem.* **1978**, *32* (283-326).

(12) Gudipati, C. S.; Finlay, J. A.; Callow, J. A.; Callow, M. E.; Wooley, K. L. The Antifouling and Fouling-Release Perfomance of Hyperbranched Fluoropolymer (HBFP)−Poly(ethylene glycol) (PEG) Composite Coatings Evaluated by Adsorption of Biomacromolecules and the Green Fouling Alga Ulva. *Langmuir* **2005**, *21*, 3044−3053.

(13) Ozaydin-Ince, G.; Matin, A.; Khan, Z.; Zaidi, S. M. J.; Gleason, K. K. Surface Modification of Reverse Osmosis Desalination Membranes by Thin-Film Coatings Deposited by Initiated Chemical Vapor Deposition. *Thin Solid Films* **2013**, *539*, 181−187.

(14) Rabe, M.; Verdes, D.; Seeger, S. Understanding Protein Adsorption Phenomena at Solid Surfaces. *Adv. Colloid Interface Sci.* **2011**, *162* (1−2), 87−106.

(15) Santos, S.; Barcons, V.; Christenson, H. K.; Billingsley, D. J.; Bonass, W. A.; Font, J.; Thomson, N. H. Stability, Resolution, and Ultra-Low Wear Amplitude Modulation Aatomic Force Microscopy of DNA: Small Amplitude Small Set-Point Imaging. *Appl. Phys. Lett.* **2013**, *103*, 063702.

(16) Guzman, H. V.; Perrino, A. P.; Garcia, R. Peak Forces in High-Resolution Imaging of Soft Matter in Liquid. *ACS Nano* **2013**, *7*, 3198−3204.

(17) Amadei, C. A.; Tang, T. C.; Chiesa, M.; Santos, S. The Aging of aSurface and the Evolution of Conservative and Dissipative Nanoscale Interactions. *J. Chem. Phys.* **2013**, *139*, 084708.

(18) Yang, R.; Buonassisi, T.; Gleason, K. K. Organic Vapor Passivation of Silicon at Room Temperature. *Adv. Mater.* **2013**, *25*, 2078−2083.

(19) Yang, R.; Gleason, K. K. Ultrathin Antifouling Coatings with Stable Surface Zwitterionic Functionality by Initiated Chemical Vapor Deposition (iCVD). *Langmuir* **2012**, *28*, 12266−12274.

(20) Wastl, D. S.; Weymouth, A. J.; Giessibl, F. J. Optimizing Atomic Resolution of Force Microscopy in Ambient Conditions. *Phys. Rev. B* **2013**, *87*, 245415.

(21) Sader, J. E; Uchihashi, T.; Higgins, M. J; Farrell, A.; Nakayama, Y.; Jarvis, S. P. Quantitative Force Measurements Using Frequency Modulation Atomic Force Microscopy—Theoretical Foundations. *Nanotechnology* **2005**, No. 16, 94−101.

(22) Giessibl, F. J. Atomic Resolution of the Silicon (111)-(7×7) Surface by Atomic Force Microscopy. *Science* **1995**, *267* (5194), 68−71.

(23) Fukuma, T.; Kobayashi, K.; Matsushige, K.; Yamada, H. True Atomic Resolution in Liquid by Frequency-Modulation Atomic Force Microscopy. *Appl. Phys. Lett.* **2005**, *87*, 034101−3.

(24) Mullen, N.; Vasilev, C.; Tucker, J. D.; Hunter, C. N.; Weber, C. H. M.; Hobbs, J. K. Torsional Tapping Atomic Force Microscopy using T-Shaped Cantilevers. *Appl. Phys. Lett.* **2009**, *94*, 173109−173109-3.

(25) Gan, Y. Atomic and Subnanometer Resolution in Ambient Conditions by Atomic Force Microscopy. *Surf. Sci. Rep.* **2009**, *64*, 99−121.

(26) Walters, D. A.; Cleveland, J. P.; Thomson, N. H.; Hansma, P. K.; Wendman, M. A.; Gurley, G.; Elings, V. Short Cantilevers for Atomic Force Microscopy. *Rev. Sci. Instrum.* **1996**, *67*, 3583−3590.

(27) Santos, S.; Guang, L.; Souier, T.; Gadelrab, K.; Chiesa, M.; Thomson, N. H. A Method to Provide Rapid in Situ Determination of Tip Radius in Dynamic Atomic Force Microscopy. *Rev. Sci. Instrum.* **2012**, *83*, 043707.

(28) Katan, A. J.; Van Es, M. H.; Oosterkamp, T. H. Quantitative Force Versus Distance Measurements in Amplitude Modulation AFM: A Novel Force Inversion Technique. *Nanotechnology* **2009**, *20*, 165703.

(29) Cleveland, J. P.; Anczykowski, B.; Schmid, A. E.; Elings, V. B. Energy Dissipation in Tapping-Mode Atomic Force Microscopy. *Appl. Phys. Lett.* **1998**, *72*, 2613−2615.

(30) Tamayo, J.; Garcia, R. Relationship Between Phase Shift and Energy Dissipation in Tapping-Mode Scanning Force Microscopy. *Appl. Phys. Lett.* **1998**, *73*, 2926−2928.

(31) Eral, H. B.; 't Mannetje, D. J. C. M.; Oh, J. M. Contact Angle Hysteresis: a Review of Fundamentals and Applications. *Colloid Polym. Sci.* **2013**, *291*, 247−260.

(32) Anand, G.; Sharma, S.; Dutta, A. K.; Kumar, S. K.; Belfort, G. Conformational Transitions of Adsorbed Proteins on Surfaces of Varying Polarity. *Langmuir* **2010**, *26*, 10803−10811.

(33) San Paulo, A.; García, R. High-Resolution Imaging of Antibodies by Tapping-Mode Atomic Force Microscopy: Attractive and Repulsive Tip-Sample Interaction Regimes. *Biophys. J.* **2000**, *78*, 1599−1605.
(34) Santos, S.; Barcons, V.; Verdaguer, A.; Font, J.; Thomson, N. H.; Chiesa, M. How Localized are Energy Dissipation Processes in Nanoscale Interactions? *Nanotechnology* **2011**, *22*, 345401.
(35) Sergio, S.; Albert, V.; Tewfic, S.; Neil, H. T.; Matteo, C. Measuring the True Height of Water Films on Surfaces. *Nanotechnology* **2011**, *22*, 465705.
(36) Garcia, R.; Tamayo, J.; San Paulo, A. Phase Contrast and Surface Energy Hysteresis in Tapping Mode Scanning Force Microscopy. *Surf. Interfaces Anal.* **1999**, *27*, 312−316.
(37) Coclite, A. M.; Shi, Y.; Gleason, K. K. Controlling the Degree of Crystallinity and Preferred Crystallographic Orientation in Poly-Perfl uorodecylacrylate Thin Films by Initiated Chemical Vapor Deposition. *Adv. Funct. Mater.* **2012**, *22*, 2167−2176.
(38) Roach, P.; Farrar, D.; Perry, C. C. Interpretation of Protein Adsorption: Surface-Induced Conformational Changes. *J. Am. Chem. Soc.* **2005**, *127*, 8168−8173.
(39) Honda, K.; Morita, M.; Otsuka, H.; Takahara, A. Molecular Aggregation Structure and Surface Properties of Poly(fluoroalkyl acrylate) Thin Films. *Macromolecules* **2005**, *38*, 5699−5705.
(40) Volkov, V. V.; Platé, N. A.; Takahara, A.; Kajiyama, T.; Amaya, N.; Murata, Y. Aggregation State and Mesophase Structure of Comb-Shaped Polymers with Fluorocarbon Side Groups. *Polymer* **1992**, *33*, 1316−1320.
(41) Kaggwa, G. B.; Kilpatrick, J. I.; Sader, J. E.; Jarvis, S. P. Artifact-Free Dynamic Atomic Force Microscopy Reveals Monotonic Dissipation for a Simple Confined Liquid. *Appl. Phys. Lett.* **2008**, *93*, 011909.
(42) Amadei, C. A.; Santos, S.; Pehkonen, S.; Verdaguer, A.; Chiesa, M. Minimal Invasiveness and Spectroscopy-Like Footprints for the Characterization of Heterogeneous Nanoscale Wetting in Ambient Conditions. *J. Phys. Chem. C* **2013**, *117*, 20819−20825.
(43) Butt, H. J.; Cappella, B.; Kappl, M. Force Measurements with the Atomic Force Microscope: Technique, Interpretation and Applications. *Surf. Sci. Rep.* **2005**, *59* (1−6), 1−152.
(44) Santos, S.; Amadei, C. A.; Verdaguer, A.; Chiesa, M. Size Dependent Transitions in Nanoscale Dissipation. *J. Phys. Chem. C* **2013**, *117*, 10615−10622.
(45) Zitzler, L.; Herminghaus, S.; Mugele, F. Capillary Forces in Tapping Mode Atomic Force Microscopy. *Phys. Rev. B* **2002**, *66*, 155436.
(46) Raj, R.; Enright, R.; Zhu, Y.; Adera, S.; Wang, E. N. Unified Model for Contact Angle Hysteresis on Heterogeneous and Superhydrophobic Surfaces. *Langmuir* **2012**, *28*, 15777−15788.
(47) Erbil, H. Y.; McHale, G.; Rowan, S. M.; Newton, M. I. Determination of the Receding Contact Angle of Sessile Drops on Polymer Surfaces by Evaporation. *Langmuir* **1999**, *15*, 7378−7385.
(48) Krishnan, S.; Paik, M. Y.; Ober, C. K.; Martinelli, E.; Galli, G.; Sohn, K. E.; Kramer, E. J.; Fischer, D. A. NEXAFS Depth Profiling of Surface Segregation in Block Copolymer Thin Films. *Macromolecules* **2010**, *43*, 4733−4743.
(49) Yaminsky, V. V., The Hydrophobic Force: the Constant Volume Capillary Approximation. *Colloids Surf., A* **1999**, *159* (181-195).